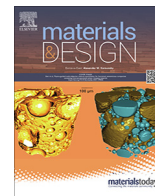




Contents lists available at ScienceDirect

Materials & Design

journal homepage: www.elsevier.com/locate/matdes

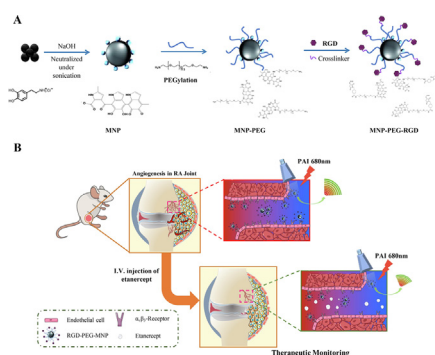
In vivo nano contrast-enhanced photoacoustic imaging for dynamically lightening the molecular changes of rheumatoid arthritis

Shuyi Xiao^{a,b}, Yufu Tang^c, Yimu Lin^a, Zhuang Lv^{d,*}, Liang Chen^{a,*}^a Department of Orthopedics, The Second Affiliated Hospital and Yuying Children's Hospital of Wenzhou Medical University, Wenzhou 325000, PR China^b Department of Pharmacy, The Second Affiliated Hospital and Yuying Children's Hospital of Wenzhou Medical University, Wenzhou 325000, PR China^c Key Laboratory of Flexible Electronics (KLOFE), Institute of Advanced Materials (IAM), Jiangsu National Synergetic Innovation Center for Advanced Materials (SICAM), Nanjing Tech University (NanjingTech), Nanjing 211816, PR China^d Department of Applied Biology and Chemical Technology, The Hong Kong Polytechnic University, Hung Hom, Hong Kong, China

HIGHLIGHTS

- We used $\alpha v\beta 3$ -targeted RGD peptide with melanin nanoparticles to enhance PAI for RA diagnosis and monitoring.
- Early RA observed by PAI was much earlier than conventional imaging techniques.
- Significant difference in MNP-PEG-RGD accumulation can be used for RA staging.

GRAPHICAL ABSTRACT



ARTICLE INFO

Article history:

Received 23 October 2020

Revised 7 March 2021

Accepted 31 May 2021

Available online 1 June 2021

Keywords:

Rheumatoid arthritis
Photoacoustic imaging
Early diagnosis
Dynamic monitoring
Therapeutic response
Melanin

ABSTRACT

Rheumatoid arthritis (RA) is one of the most prevalent inflammatory joint disorders. Early diagnosis, accurate staging, and imaging guided treatment response of RA remain crucial clinical significances for improving treatment outcomes. In this study, we introduced endogenous melanin nanoparticles (MNPs) conjugated with Cyclic Arg-Gly-Asp (RGD) peptide (MNP-PEG-RGD) as a contrast agent for accurate photoacoustic imaging (PAI) of RA diagnosis. It was observed that the prepared nanoprobe had favorable PA sensitivity, photostability and biocompatibility. *In vivo* studies using RA mouse model revealed that this nanoprobe could target $\alpha v\beta 3$ actively at 1 h post-injection, while the signal was remarkably increased in the arthritic joint which could earlier diagnose RA than conventional imaging system. It was of crucial importance to staging RA by PAI with significant difference in nanoprobe accumulation. Furthermore, we tracked the therapeutic efficacy of etanercept in RA treatment by PAI. The observed advancement of arthritis on the PAI was confirmed by histological and immunohistochemical analysis. In conclusion, this study shed light on the development of innovative multifunctional theranostic nanoplatform for both RA monitoring and treatment with a promising future in clinical translation.

© 2021 The Authors. Published by Elsevier Ltd. This is an open access article under the CC BY-NC-ND license (<http://creativecommons.org/licenses/by-nc-nd/4.0/>).

1. Introduction

Rheumatoid arthritis is a prevalent autoimmune joint disease characterized by autoantibody productions, persistent synovitis, pannus formation, and joint destruction. It can cause cartilage

* Corresponding authors at: Hung Hom, Hong Kong, China (Z. Lv), 109 Xueyuan West Road, Wenzhou 325027, PR China (L. Chen).

E-mail addresses: 176819308@qq.com (Z. Lv), breakingsunshine@163.com (L. Chen).

and bone destruction, leading to progressive disability, systemic complications, and worldwide socioeconomic burden. One of the limiting factors to an ideal therapeutic response is the delay in RA diagnosis in clinics. Early RA (ERA) was proposed with the concept that the diagnosis is given early within the first weeks or months of joint symptoms or signs [1]. It renders a time span for proper therapeutic treatment, which may improve clinical outcomes [2]. In order to achieve the clinical success of ERA, the technical requirements and demands are continuously increased.

Imaging plays a prominent role in the diagnosis and treatment monitoring of RA. Clinical imaging modalities for RA usually include radiography, ultrasound and magnetic resonance imaging (MRI). However, the lack of sensitivities and accuracies in findings also limits current imaging modalities in early diagnosis of RA [3]. Molecular imaging has attracted numerous attentions in health care. It visualizes, characterizes and measures biological process in cellular and subcellular levels in disease. Molecular imaging also monitors pathological progression as well as therapeutic response in a minimal invasive manner. In comparison to traditional imaging modalities, molecular imaging allows earlier treatment interventions as it can not only detect lesions but also determine the nature of earlier targets more precisely [4–6]. Photoacoustic imaging (PAI) is an emerging molecular imaging mode, which takes advantages of weak acoustic scattering in tissues while retains the high biological penetration and contrast characteristic of optics [7,8]. When coupled with multispectral near-infrared (NIR) excitation and by converting from photons to ultrasonic waves, PAI can provide high spatial resolution (~150 μm) with a great depth (>5 cm) [9–11]. In addition, PAI has well detection sensitivity because it can identify both intrinsic chromophores (hemoglobin, melanin...) and exogenous molecules [12–14]. The outstanding performances of PAI, including non-ionizing radiation, non-invasive as well as real-time monitoring, qualifying it as a promising modality for preclinical investigations and further in translation into clinical use [15–17].

To date, nanoparticle-based PA contrast agents have been extensively studied to enhance the contrast ratio and specificity of imaging [18–20]. The nanomaterials used for contrast can be roughly divided into inorganic and organic agents. The most common inorganic materials are gold nanoparticles, single-wall carbon nanotubes (SWCNTs) and graphenes. But the primary disadvantages of inorganic nanomaterials are low biocompatibility and poor photostability [21–23]. Besides, SWCNTs also face the issue of non-specific peak in absorption spectrum [24]. Organic nanomaterials have been widely investigated in PAI due to their great biodegradability and biocompatibility, and excellent optical properties. Melanin is an endogenous natural pigment with intrinsic NIR absorption as well as favorable stability under physiological conditions [25,26]. Recently, it has been reported the applications of melanin-based nanoparticles in PAI by utilizing the extensive NIR absorption of melanin, showing superb chelating performance, excellent contrast capability in living systems and prospective biocompatibility, which makes it a satisfactory nanoplatform for diagnosis and monitoring [27–31].

Angiogenesis is a critical factor in the occurrence stage of RA and is involved in the disease progression [32]. It is widely accepted that $\alpha_v\beta_3$ -integrin is largely upregulated on vascular endothelial cells (VECs) in inflammation sites [33,34]. Meanwhile, it is known that arginine-glycine-aspartic acid (RGD) peptide can be specifically recognized by $\alpha_v\beta_3$ -integrin [35–37]. A potential alternative delivery approach in RA is to target angiogenesis or new blood vessel growth. Building upon these, we strategically conjugated RGD onto the surface of water-soluble melanin nanoparticles (MNPs) as an active targeting moiety for angiogenic knee joint. In this study, we created a new RA imaging system

using MNP-PEG-RGD as a PAI-enhanced nanoplatform. We assessed the PA contrast characterization of MNP-PEG-RGD and discussed the feasibility for future clinical translations. In living mouse models after intravenous injection, MNP-PEG-RGD exhibited about 3.36-fold stronger PA signal in RA joint (with $\alpha_v\beta_3$ -overexpression) than normal joint. Furthermore, the obtained PAI offered the accurate information of different RA stages. Meanwhile, it intuitively performed RA therapeutic response of etanercept with the reduced PA signal intensity. Consequently, we can clearly distinguish the staging of RA and track the therapeutic outcomes in RA after drug treatment. All PAI results were examined histologically and immunohistochemically.

2. Materials and methods

2.1. 1 Synthesis of MNP-PEG-RGD

The MNP-PEG-RGD were fabricated based on a published protocol [31]. In brief, water soluble MNPs were obtained from 20 mg tyrosine-derived synthetic melanin sufficiently dissolved 0.1 N NaOH aqueous solution and 0.1 N HCl aqueous solution was used for adjusting the pH to 7.0. Then NH_4OH solution was added into MNPs aqueous solution (5 ml, 1 mg/mL of deionized water) to adjust the pH to 9.0. The mixed solution was slowly added dropwise into $\text{NH}_2\text{-PEG}_{5000}\text{-NH}_2$ for 12 h under vigorous stirring to obtain PEGylated MNPs. To obtain the final product of MNP-PEG-RGD, the cross-linker solution was first prepared with 1.2 mg of 4-(N-maleimidomethyl)cyclohexane-1-carboxylic acid 3-sulfo-N-hydroxysuccinimide ester sodium salt (sulfo-SMCC) dissolved in 36 μL of dimethyl sulfoxide (DMSO). At ambient temperature, MNP-PEG [1 mg/mL of PBS (pH = 7.2)] was incubated with the above cross-linker solution for 2 h. After running through a PD-10 column and concentrated, the thiol-active MNP was obtained to a final volume of 0.5 ml. The cRGDFc stock solution (120 μL of 5 mM in the degassed water) was added to the above MNP solution with stirring for 24 h at 4 $^\circ\text{C}$. The unreacted RGD was removed using a PD-10 column and was collected to quantify the amount by High Performance Liquid Chromatography (HPLC). The final MNP-PEG-RGD were obtained. Following the same procedure, cyclic Arginine-Alanine-Aspartic acid (RAD) peptide was conjugated to MNP-PEG as non-specific nanoparticles (MNP-PEG-RAD).

2.2. Characterization of MNP-PEG-RGD

The morphology and size of MNP-PEG-RGD were measured by transmission electron microscope (TEM) and dynamic light scattering (DLS). Zeta potentials were determined by zeta potential analyzer (Malvern, Zetasizer Nano, ZS90). Ultraviolet–visible (UV–vis) absorption spectroscopy of MNP-PEG-RGD was processed in a UV–Vis spectrophotometer. In this work, the 680 nm wavelength was used as the NIR laser source for the PAI study. Under continuous laser irradiation at 680 nm and $0.5\text{W}/\text{cm}^2$ for an hour, MNP-PEG-RGD was tested for the photostability. To further study the detection sensitivity of PA signal in living body by MNP-PEG-RGD, 100 μL of MNP-PEG-RGD aqueous solution with different concentrations, mixed with matrigel, were subcutaneously injected on the lower back of mice. The PA signals were collected after they were solidified and analyzed by Endra Nexus 128 (Endra, Inc., Ann Arbor, MI) PAI system. Regions of interest (ROIs) (indicated as white dashed circle, diameter: 2.5 mm) were drawn each PA image and were analyzed by Osiris imaging software (OsiriX Foundation, Genève, Switzerland). Before injection contrast agent, the background signal from tissue was quantified.

2.3. PAI system characterization

In this study, Endra Nexus 128 PAI system was used with a tunable laser wavelength from 680 to 950 nm. This instrument is equipped with a repetition rate of 20 Hz as well as a pulse width of 7 ns, a spatial resolution of 250 μm and a volume pixel resolution of 100 μm . The laser has a 8 mJ/pulse output energy on the sample surface, which is well below the safety standard set by American National Standard Institute (ANSI) [38]. PA signals were received by 128 identical ultrasonic transducers with the center frequency of 5.8 MHz. Regions of interest (ROIs) (4 mm \times 6 mm) were drawn on each PA image and were analyzed by Osirix imaging software (OsiriX Foundation, Genève, Switzerland).

2.4. *In vitro* viability

In vitro cytotoxicity of MNP-PEG-RGD was determined by MTT assay in NIH3T3 fibroblast cells, which were used as a normal control to evaluate the cytotoxicity of nanoparticles as well as the therapeutic effect of nanomedicine in previous studies [39]. In brief, NIH3T3 fibroblast cells were seeded into 96 well plates at a density of 5×10^4 cells per cm^2 . The cells were co-cultured with gradient concentrations of 0–100 $\mu\text{g mL}^{-1}$ MNP-PEG-RGD for 24 h and 48 h, respectively. 20 μL of MTT solution was added into each well to produce formazan crystals. After 4 h of incubation, the supernatant was removed and 200 μL of dimethyl sulfoxide (DMSO) was added to dissolve the formed precipitates. The light absorption (OD) values were recorded at 490 nm with the microplate spectrophotometer.

2.5. Targeting property of MNP-PEG-RGD *in vitro*

In vitro targeting property of MNP-PEG-RGD was assessed on human umbilical vein endothelial cells (HUVECs), which were $\alpha_v\beta_3$ over-expression according to previous studies [40,41]. HUVECs were obtained from Shanghai Institute of Cell Biology and cultured in Endothelial Cell Growth medium EBM-2 medium containing growth factors (Clonetics, Lonza, Verviers, Belgium). All culture media were supplemented with 10% fetal bovine serum (FBS) and 100 IU/mL penicillin and 100 $\mu\text{g/mL}$ streptomycin sulfate. The cells were incubated at 37 $^\circ\text{C}$ and 5% CO_2 , in a humidified atmosphere during culture as well as during the experiments. HUVECs were seeded in the coated wells at a density of 10,000 cells/well and incubated overnight at 37 $^\circ\text{C}$. Next, the cell medium was refreshed and MNP-PEG-RGD dispersed in PBS were added to the cells at a final concentration of 0.5 mg mL^{-1} . The cells were incubated with the MNP-PEG-RGD for 60 min then washed with PBS for further PAI. As comparison, MNP-PEG-RAD, PBS, pure HUVECs aggregation and the blocking group (pre-incubated with excess cRGD for 60 min) were also subjected to the same procedure.

2.6. Establishment of RA models

Female Kunming mice (8-week old) were purchased from Experimental Animal Center of Wenzhou Medical College. All animal experiments were performed following the protocol approved by the Animal Ethics Committee of the institution and the Guidelines for Animal Experimentation of Wenzhou Medical University. The antigen-induced arthritis (AIA) mouse model was established according to the previously described standard protocol [42,43]. Briefly, twenty microliters complete Freund's adjuvant were injected below the right knee of each mouse.

2.7. *In vivo* PA imaging

To validate the contrast ability of MNP-PEG-RGD in RA joints, RA mice were administrated with 100 μL of MNP-PEG-RGD (1 mg mL^{-1}) through tail vein at day 12 post induction of AIA and the RA joints were imaged to compare with the normal joints (injected with PBS) in PAI. Next, the targeting ability of MNP-PEG-RGD towards neovascular in RA joints was examined. RA mice intravenous (i.v.) injected with 100 μL of probes (MNP-PEG, MNP-PEG-RAD, 1 mg mL^{-1}) for *in vivo* PAI from 0 to 24 h post injection. Before injection, the hair on the hind limbs of mice were removed by commercial hair-removal lotion. During the imaging process, mice were anesthetized with 3% isoflurane and the knee joint (imaging target) with moderate stretched was kept consistent at the bottom of the bowl to facilitate comparison (Fig. S2), and *in vivo* manner of MNP-PEG-RGD were whole process monitored. In order to maintain measurement consistency, we chose three landmarks, which were as follows: the center of knee joint (Fig. S2. red circle), tibial tubercle (Fig. S2. blue circle) and saphenous vein (Fig. S2. red curve). For reproducible positioning of the animals between measurements, the knee joint (imaged target) was placed at the bottom of the bowl and the 3 landmarks were placed at the same position at the bottom of bowl (mark the bottom of the bowl after positioning). In order to provide favorable PA signal transduction, no bubble was allowed on the imaging target. The PAI system was set at 680 nm wavelength to precede imaging. The ROI was drawn on each PA image and the mean PA intensity was calculated by Osirix imaging software.

To evaluate whether MNP-PEG-RGD-enhanced PAI enables distinguish developed stage of RA from early stage of RA, MNP-PEG-RGD was i.v. injected in the mice at day 12 and 28, respectively, and transferred for PAI. The mice were also imaged with X-ray and MRI. After 24 h of PAI, mice were sacrificed, and the knee joints were harvested for histological and immunohistochemical examinations. Using these two different stages of RA mice, we further investigated the monitoring ability of MNP-PEG-RGD on therapeutic efficacy of etanercept (Enbrel[®]), which is an anti-tumor necrosis factor medication in clinics to manage RA. In this experiment, starting from day 12 post AIA induction, 100 μL of etanercept (0.3 mg/kg) was intramuscularly injected into RA mice with a constant interval of four days. After the course of treatment, mice were i.v. injected with MNP-PEG-RGD for sequential PAI.

2.8. *In vivo* X-ray and MRI

X-ray examination was performed by X digital imaging system (MX-20, Faxitron, and American) for small animal for knee joint. *In vivo* T2-weighted MR images were collected using a 7.0 T micro-MRI system (Bruker, Germany) with isoflurane inhalation. The specific parameters of MRI were set as follows: repetition time (TR) = 3698.9 ms, echo times (TEs) = 45 ms, field of view (FOV) = 40 \times 40 mm, slices = 30, slice thickness (ST) of 1 mm, flip angle (FA) = 180 $^\circ$, acquisition time (TA) = 15 min 46 s. T₂ images were processed with the Image Sequence Analysis Tool of Bruker Paravision 5.1 (Bruker Biospin, Ettlingen, Germany).

2.9. Histopathology and immunohistochemistry (IHC)

After *in vivo* imaging, mice were euthanized and sacrificed at different week-points post-injection. The knee joints were collected for histopathological examination and preserved in 4% paraformaldehyde overnight. The joints were decalcified in 10% EDTA for 6 days, and subsequently the specimens were embedded into paraffin. The joint tissues were sectioned into 4 μm of each slice and stained with hematoxylin and eosin (H&E) as well as toluidine blue (TB) to evaluate the morphology changes of knee joint

and cartilage damage. The joint sections were also stained for immunostaining of $\alpha_v\beta_3$ to verify the expression of $\alpha_v\beta_3$. Histological scoring was detailed in supporting information.

In order to estimate the systemic side effect, the body weights of the mice were measured, and main organ tissues (including heart, spleen, lung, liver and kidney) were extracted at 1 and 7 days after i.v. injection of PBS or MNP-PEG-RGD (1 mg ml⁻¹, 100 μ L). To analyze toxicity in local knee joint, mice were intra-articularly injected with 10 μ L of MNP-PEG-RGD (1 mg ml⁻¹) and joints were harvested 3 days after injection for H&E staining. Tissue sections were prepared as mentioned above and dyed with H&E.

2.10. Statistical analysis

All experimental data were statistically analyzed by means of GraphPad software (GraphPad Software, Inc., La Jolla, CA, Version

6.0d) and presented as mean \pm standard deviation (SD). Correlation coefficient was determined using linear regression and by calculating Pearson correlation coefficient (r). Statistical analysis was performed using Student's t -test and statistical significance was set at $p < 0.05$.

3. Results and discussion

3.1. Preparation and characterization of MNP-PEG-RGD

The synthesis procedure was schematically illustrated in Fig. 1A. As shown in Fig. 1B, the as-prepared MNP-PEG-RGD had a spherical shape with high monodispersity in aqueous solution, which can be attributed to the negative charges of about -10.6 ± 4.2 mV on the surface of these nanoparticles that efficiently blocked particle aggregation through electrostatic repulsion

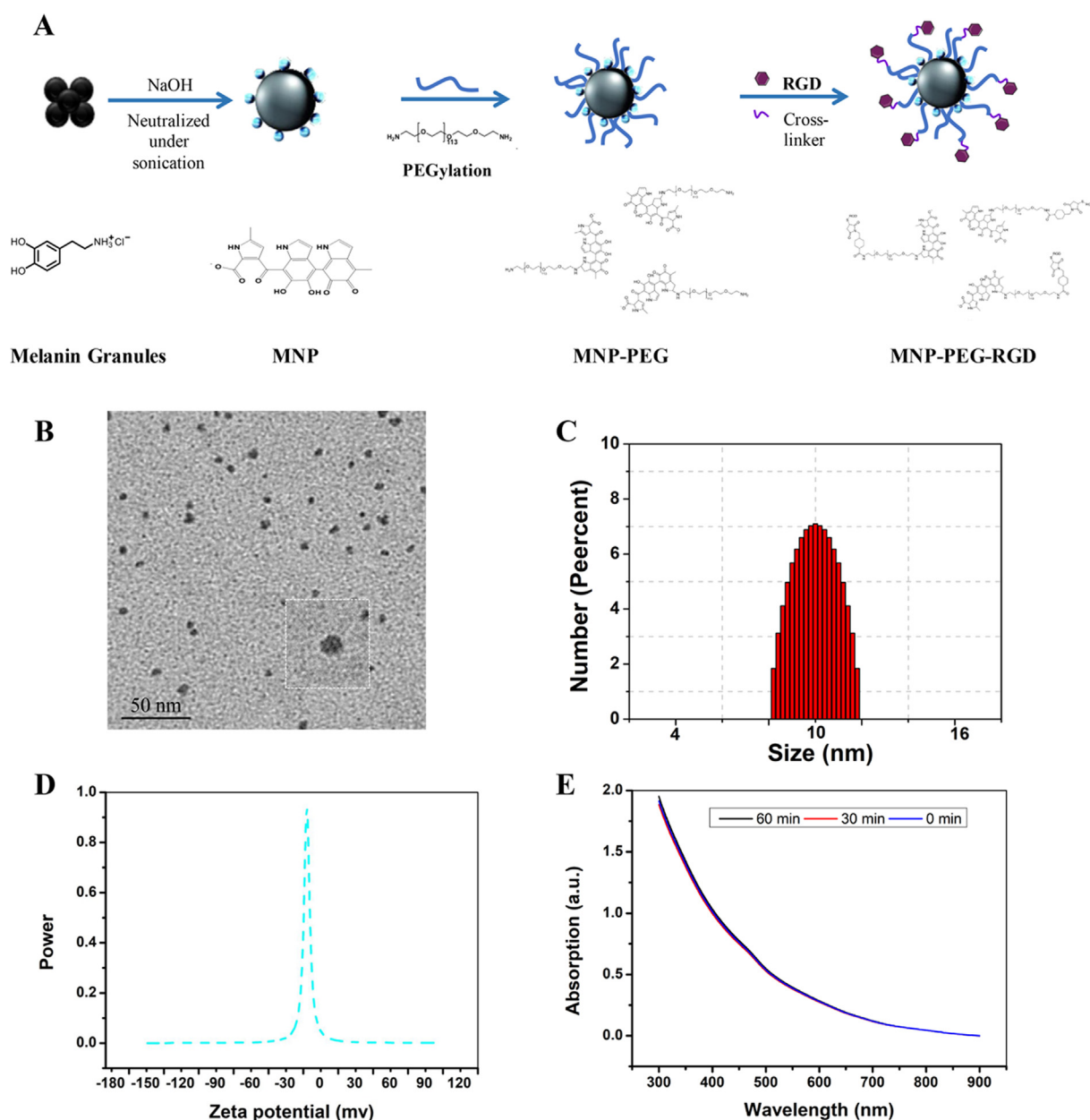


Fig. 1. Characterization of MNP-PEG-RGD. (A) The synthesis procedure of MNP-PEG-RGD was schematically illustrated. (B) TEM image of MNP-PEG-RGD. Scale bar is 50 nm. (C) DLS of MNP-PEG-RGD. (D) Zeta potential of MNP-PEG-RGD. (E) Photobleaching test: UV-vis-NIR absorption spectra of MNP-PEG-RGD solution exposure under 680 nm laser irradiation (8 mJ cm⁻²) of 0, 30 and 60 min.

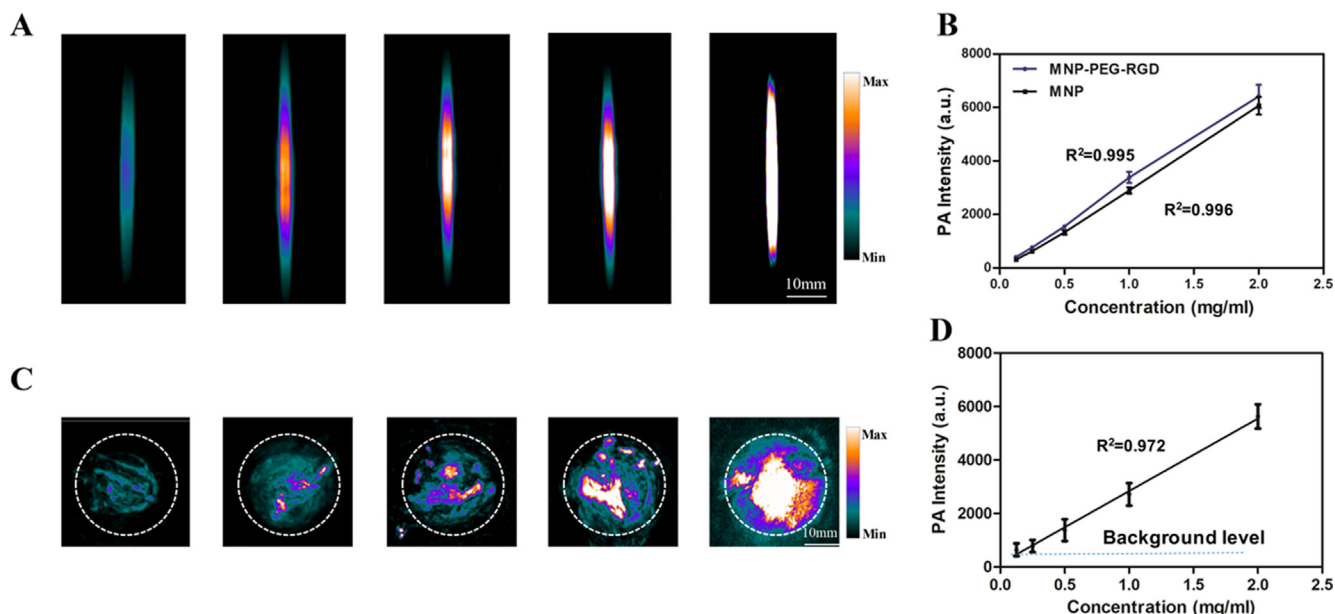


Fig. 2. *In vitro* PA property and *in vivo* PA sensitivity of MNP-PEG-RGD. (A) The PA images of MNP-PEG-RGD in aqueous solution at concentrations of 0.125, 0.25, 0.5, 1.0, 2.0 mg ml⁻¹. The scale bar is 10 mm. (B) The PA intensities of MNP-PEG-RGD and MNP were both found to be linearly dependent on its concentration ($R^2 = 0.995$, $R^2 = 0.996$). (C) The PA images of MNP-PEG-RGD in living mice which were subcutaneously injected on the back of mice at concentrations of 0.125, 0.25, 0.5, 1.0, 2.0 mg ml⁻¹. The scale bar is 10 mm. (D) The PA signal from each inclusion was calculated. The background level represents the endogenous signal measured from tissues. The linear regression is calculated on the five most concentrated inclusions ($R^2 = 0.972$).

(Fig. 1C). DLS analysis showed the hydrodynamic diameter of MNPs was approximately 4.8 ± 1.4 nm, which also showed spherical morphology in TEM (Fig. S1). The diameter of MNP-PEG-RGD became larger after modification with a size of 9.7 ± 2.6 nm in PBS (Fig. 1B). The average number of RGD attached per MNP-PEG was about 8 calculated by HPLC (the detailed calculation was shown in Supporting information). In this study, 680 nm was chosen as the NIR laser source for the following PAI study based on the previous study [31]. Under continuous laser irradiation, the optical stability of MNP-PEG-RGD was further tested, which showed excellent photostability at $0.5\text{W}/\text{cm}^2$ for 1 h (Fig. 1D).

To investigate the feasibility of MNP-PEG-RGD as a PA contrast agent, PA signal was first detected in aqueous solutions with concentrations ranging from 0.125 to 2 mg mL⁻¹ at 680 nm (Fig. 2A). A linear correlation ($R^2 = 0.995$) between the enhancement of the PA signal intensities and the increase concentrations of MNP-PEG-RGD was observed similar to the result of MNP ($R^2 = 0.996$)

(Fig. 2B), which indicated that no significant aggregation occurred during synthesis and the contrast ability of MNP-PEG-RGD had a minimal influence by RGD complexation. Meanwhile, the PA detection sensitivity of MNP-PEG-RGD at 680 nm was around 0.125 mg mL⁻¹ (Fig. 2B). To further evaluate the PA sensitivity of MNP-PEG-RGD in living body, 100 μL of MNP-PEG-RGD with concentrations from 0.125 to 2 mg mL⁻¹ were mixed with matrigel and were subcutaneously injected on the back of mice. The corresponding PA signals were observed in PA images (Fig. 2C). The background signal from tissue was determined without any injections of contrast agent, and 0.125 mg mL⁻¹ of MNP-PEG-RGD were found to perform an equivalent PA signal intensity compare to the tissue background (Fig. 2D). A concentration-dependent manner was shown in Fig. 2C that PA signal strength increased linearly with the increase of MNP-PEG-RGD concentrations. More importantly, the slope of regression line proved the great sensitivity of PAI to the content changes of MNP-PEG-RGD ($R^2 = 0.972$). These results demonstrated the huge potential of MNP-PEG-RGD as an *in vivo* PA nanoprobe.

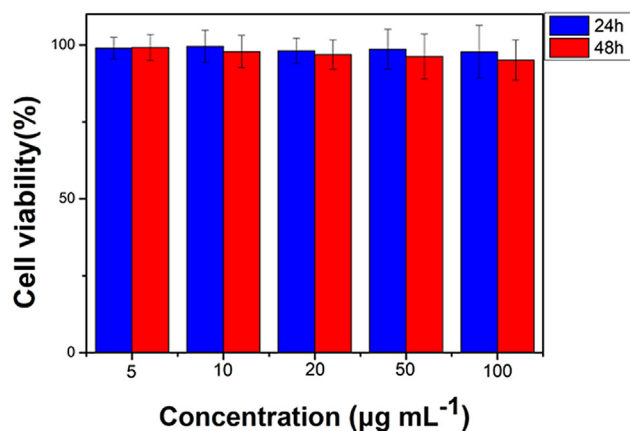


Fig. 3. Cytotoxicity assessment of MNP-PEG-RGD. NIH3T3 fibroblast cells were treated with MNP-PEG-RGD for 24 and 48 h respectively and the cell viability was measured by MTT assay.

3.2. *In vitro* cytotoxicity

MTT assay was carried out on NIH3T3 cells to quantitatively test the viability of cells in increasing concentrations of MNP-PEG-RGD. It was noteworthy that no observable cytotoxicity was detected in MNP-PEG-RGD up to 100 $\mu\text{g mL}^{-1}$ against NIH3T3 cells and retained over 90% viability at 24 h and 48 h after treated with the nanoprobe, suggesting the promising safety of MNP-PEG-RGD *in vitro* (Fig. 3).

3.3. Targeting ability of MNP-PEG-RGD *in vitro*

Representative *in vitro* PAI of all groups were showed in Fig. 4A. After incubation with MNP-PEG-RGD, the PA signal intensity of HUVECs in MNP-PEG-RGD group was 4 times as MNP-PEG-RAD group (Fig. 4). The difference of PA signal intensity should be due to the specific interaction between the integrin $\alpha_v\beta_3$ protein

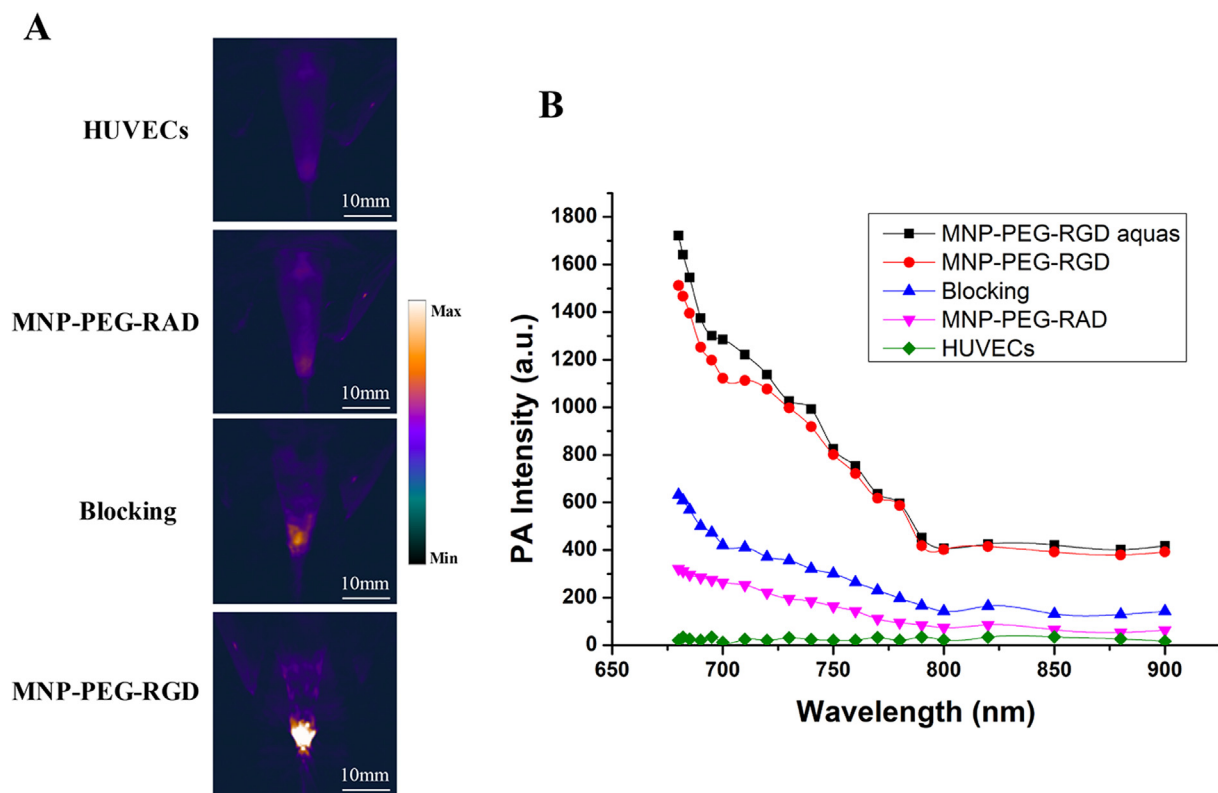


Fig. 4. *In vitro* targeting assessment of MNP-PEG-RGD to HUVECs with $\alpha_v\beta_3$ overexpression. (A) Representative PA images of HUVECs before and after incubation with different nanoprobes (MNP-PEG-RAD, blocking and MNP-PEG-RGD, 0.5 mg mL^{-1}). The scale bar is 10 mm. (B) PA spectrum of MNP-PEG-RGD in aqueous solution and treated HUVECs.

HUVECs and RGD on the surface of MNP-PEG. The blocking experiment was further conducted to verify the targeting property of MNP-PEG-RGD. HUVECs were pre-incubated with RGD for 60 min, then treated with MNP-PEG-RGD. The PA signal intensity of HUVECs treated with pure MNP-PEG-RGD was 2.4 times higher than that of HUVECs pre-incubated with RGD. We further used PA spectra to differentiate whether the PA signal of interest induced from the contrast or the background in the NIR region. Moreover, the PA spectra of the related HUVECs in the MNP-PEG-RGD group (Fig. 4) had a similar profile to the MNP-PEG-RGD in aqueous solution, demonstrating that the enhanced PA signal in the cells was derived from the absorbed MNP-PEG-RGD. All these results demonstrated that MNP-PEG-RGD can specifically enhance PAI through the integrin $\alpha_v\beta_3$ mediated cellular binding and uptake.

3.4. Clinical findings

Based on our pre-experiment and in accordance to previous study, mice exhibited slight signs of arthritis at 12–14 days post induction of AIA, including neutrophils infiltration and synovitis, without obvious destruction of cartilage and bone, which was indicated as early stage of RA in the following study. At day 28–35, all the mice developed severe arthritis including swelling, redness, increased neutrophils infiltration and obvious cartilage erosion in histological analysis [44,45]. This time point was studied as developed stage.

3.5. *In vivo* imaging results of MNP-PEG-RGD for RA by PAI

Building upon the advantages of PAI for *in vivo* diagnosis and the favorable *in vitro* PAI results with high sensitivity and rich contrast, we hypothesized that MNP-PEG-RGD can serve as an active-

targeting PA nanoprobe for RA, guiding ERA formation and further for treatment response. To verify these, we first determined the diagnosis and homing ability of MNP-PEG-RGD *in vivo*. The AIA mice were used in this study. At 12 days after the induction of AIA, mice were *i.v.* injected with $100 \mu\text{L}$ of MNP-PEG-RGD by PAI. RA mice (Right knee joint: RA; Left knee joint: Normal) were imaged at various time points after injection. Due to endogenous chromophores (hemoglobin and calcium content), only tibia and saphenous vein in joint region were imaged with low contrast (681 ± 76) during pre-injection scans (indicated as “0 h”, Fig. 5A). Compared with previous study of PA imaging, like using L-selectin/P-selectin-targeting contrast agent, we can clearly observe the structure of the knee joint by MNP-PEG-RGD-enhanced PAI, such as saphenous vein and tibia, which helped us accurately locate the interested region (indicated as white dashed oval in Fig. 5A) without the need for additional imaging modalities [45].

In order to determine the RA diagnosis potential of MNP-PEG-RGD, the healthy and RA knee joints were imaged representatively by PAI after injection of MNP-PEG-RGD. Representative PA images post-injection at 1, 3 and 24 h were shown in Fig. 5A. In the RA knee joint region, strong PA signal was clearly displayed after injected with MNP-PEG-RGD, which was also confirmed by quantitative analysis of identical ROI (indicated as white dashed oval) in Fig. 5B. The PA signal intensity from MNP-PEG-RGD injected RA mice significantly increased during the initial 3 h and was maximized to 2301 ± 187 , indicating the gradual accumulation of MNP-PEG-RGD in RA joint. Additionally, the accumulation of MNP-PEG-RGD in desired place *in vivo* (knee joint) was also confirmed by the similar PA spectra trend displayed in knee joint and aqueous solution, but much different from that injected with PBS (Fig. 5D). This time point, 3 h post-injection, was chosen as a proper image time point in the following study. Then the PA signal

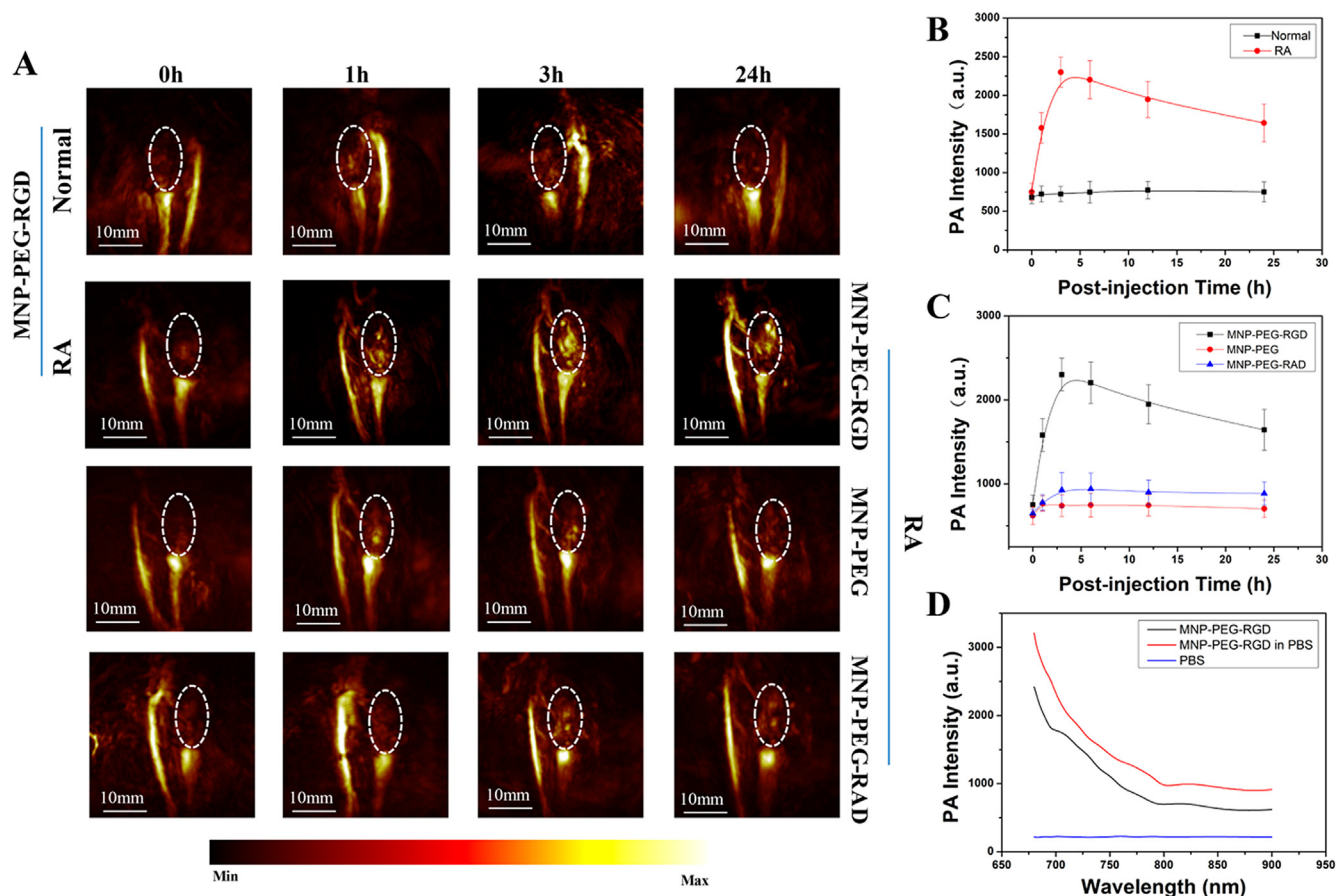


Fig. 5. The diagnosis and targeting potential of MNP-PEG-RGD in RA mice. (A) Representative PA images of knee joints before and after injection of nanoprobes at different imaging points. Row 1 was the group of normal knee joint injected with MNP-PEG-RGD, row 2 was the group of RA knee joint injected with different nanoprobes. The scale bar is 10 mm. (B) The corresponding PA signal intensities between normal and RA knee joints after i. v. injection of MNP-PEG-RGD. (C) The corresponding PA signal intensities among MNP-PEG-RGD, MNP-PEG-RAD and MNP-PEG of RA knee joints after i.v. injection. (D) PA spectra of MNP-PEG-RGD (1 mg mL^{-1}) in PBS and MNP-PEG-RGD in RA knee joint at 3 h after injection *in vivo*. PA spectra of PBS. Error bars in B and C represent standard deviation ($n = 5/\text{group}$).

gradually reduced and reached a plateau (Fig. 5B). As for the normal knee, no obvious signal enhancement was observed during the whole imaging process. Compared between normal and RA knee joints, PA signal intensity was remarkably increased in RA joint post-injection at 3 and 6 h ($p < 0.01$). It remained fairly steady in the following 18 h, the PA signal intensity was about 3.36 times higher than that from normal joints ($p < 0.05$), which suggested that MNP-PEG-RGD were able to diagnosis RA as it can efficiently distinguish RA joints from normal joints at early stage via remarkable signal difference.

To confirm the MNP-PEG-RGD's ability to target $\alpha_v\beta_3$ *in vivo*, MNP-PEG-RAD and PEGylated MNP were used as control contrasts for PAI. In Fig. 5A, compared with pre-scan, it was distinct that no obvious increase of signal intensity was found in RA mice administrated with control MNP-PEG-RAD or MNP-PEG. We further quantitatively analyzed the statistical significance between RA groups (administrations of MNP-PEG-RGD, MNP-PEG-RAD and MNP-PEG, respectively) at different image time points. The outstanding difference exhibited in time-PA intensity curves revealed the neo-vessel targeting ability of MNP-PEG-RGD through RGD (Fig. 5C). Therefore, the diagnostic ability of MNP-PEG-RGD in RA can be attributed to the pathologic state of RA that neo-vascular was formed in RA knee joint [46]. These results demonstrated that MNP-PEG-RGD possessed superb *in vivo* PAI capability for accurately diagnosis of RA with specific targeting property via $\alpha_v\beta_3$ -targeted.

In the following study, we evaluated the feasibility of MNP-PEG-RGD to distinguish different stages of RA in comparison with the classic staging methods. Experimental timeline was depicted in Fig. 6A. The stages were clarified as non-inflammation, slight inflammation and severe inflammation by histological examinations including H&E and TB staining. No sign of inflammation was showed in normal mice without RA induction, the integrity of cartilage and bone was preserved (Fig. 7A). Though cartilage remained relatively intact in the early stage of RA, the infiltration of neutrophils was observed (Fig. 7B, $p < 0.01$). The above findings also confirmed that the ability of MNP-PEG-RGD to accurately diagnosis RA in the early stage with slight inflammation by performing strong signal intensity (Fig. 5A & B). At 28 days after AIA induction, the degree of angiogenesis was augmented [47], which resulted in an increased PA signal (shown in Fig. 5B). The PA signal ratio of the developed RA to early RA reached the highest value of about 1.766 at 3 h after injection and retained steady over time (Fig. 6D). Mice exhibited severe inflammation in PAI were found to have extended clinical symptoms in histological examinations. In comparison to early stage, RA mice in the developed stage exhibited considerably cartilage erosion (Fig. 7B, $p < 0.001$) with remarkably increased neutrophils infiltration (Fig. 7C, $p < 0.001$), making it hard to distinguish the interface between the bone and cartilage (Fig. 7A). Additionally, RA mice showed more pronounced joint space narrowing and the inflamed synovium invaded into the joint in the developed stage. These histological characters were consis-

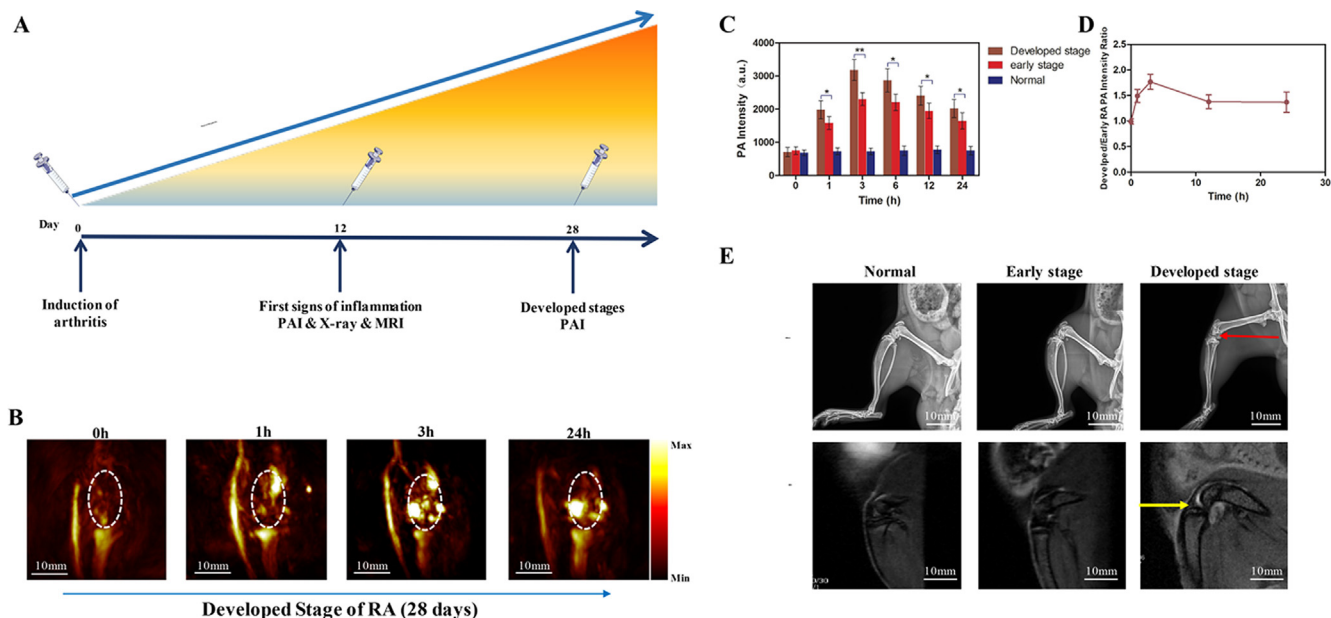


Fig. 6. *In vivo* distinguishing the stages of RA by MNP-PEG-RGD-enhanced PAI. (A) Schematic illustration of experimental timeline. (B) Representative PA images of developed RA knee joints before and after injection of MNP-PEG-RGD (1 mg mL⁻¹) at different imaging points. The scale bar is 10 mm. (C) The corresponding PA signal intensities among normal, early and developed RA after i.v. injection of MNP-PEG-RGD (1 mg mL⁻¹). (D) PA intensity ratios (developed RA joint vs. early RA joint) from MNP-PEG-RGD. Error bars in C and D represent standard deviation (n = 5/group). (E) X-ray and MRI images of different stages of RA knee joints. The red arrow indicated a few osteophyte formations, the yellow arrow indicated the thickened synovial membrane and joint effusion. The scale bar is 10 mm.

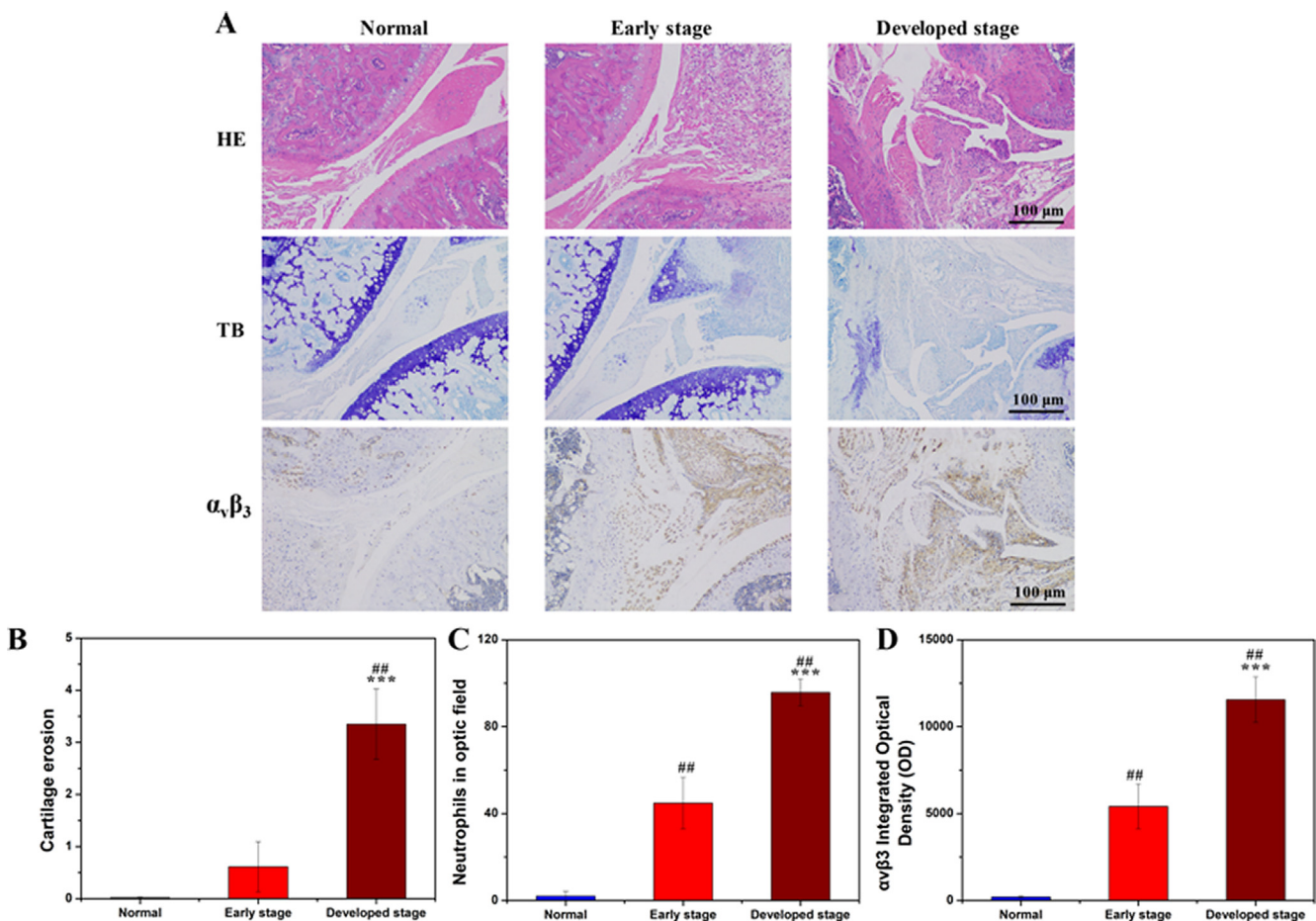


Fig. 7. Histological analysis of RA severity and IHC of $\alpha_v\beta_3$ -integrin expression. (A) Representative mice joints histologic appearance of H&E and TB staining of normal and RA knee joints. IHC of $\alpha_v\beta_3$ -integrin. All the scale bar is 100 μ m. Histological scores of (B) cartilage erosion and (C) neutrophils infiltration are shown. (D) $\alpha_v\beta_3$ integrated optical scores for each group. Error bars in B, C, D represent standard deviation (n = 5/group). *** is $p < 0.001$. ## is $p < 0.01$.

tent with published researches [48–50]. Statistically significant difference between early RA and developed RA was analyzed at each imaging point (Fig. 6C). Notable difference between the three groups clearly suggested that MNP-PEG-RGD-enhanced PA could sensitively diagnose different stages of RA through the PA signal variations in the knee joint region. However, we did not find dis-

tinct pathological or structural changes of knee joint with slight inflammation in subsequent X-ray and MRI inspections in the ERA (Fig. 6E). But osteophyte formation in the developed stage was detected in X-ray (indicated by red arrow in Fig. 6E). In addition, we observed joint effusion, synovial membrane thickness in the developed stage of RA by MRI. Given the limitation of standard

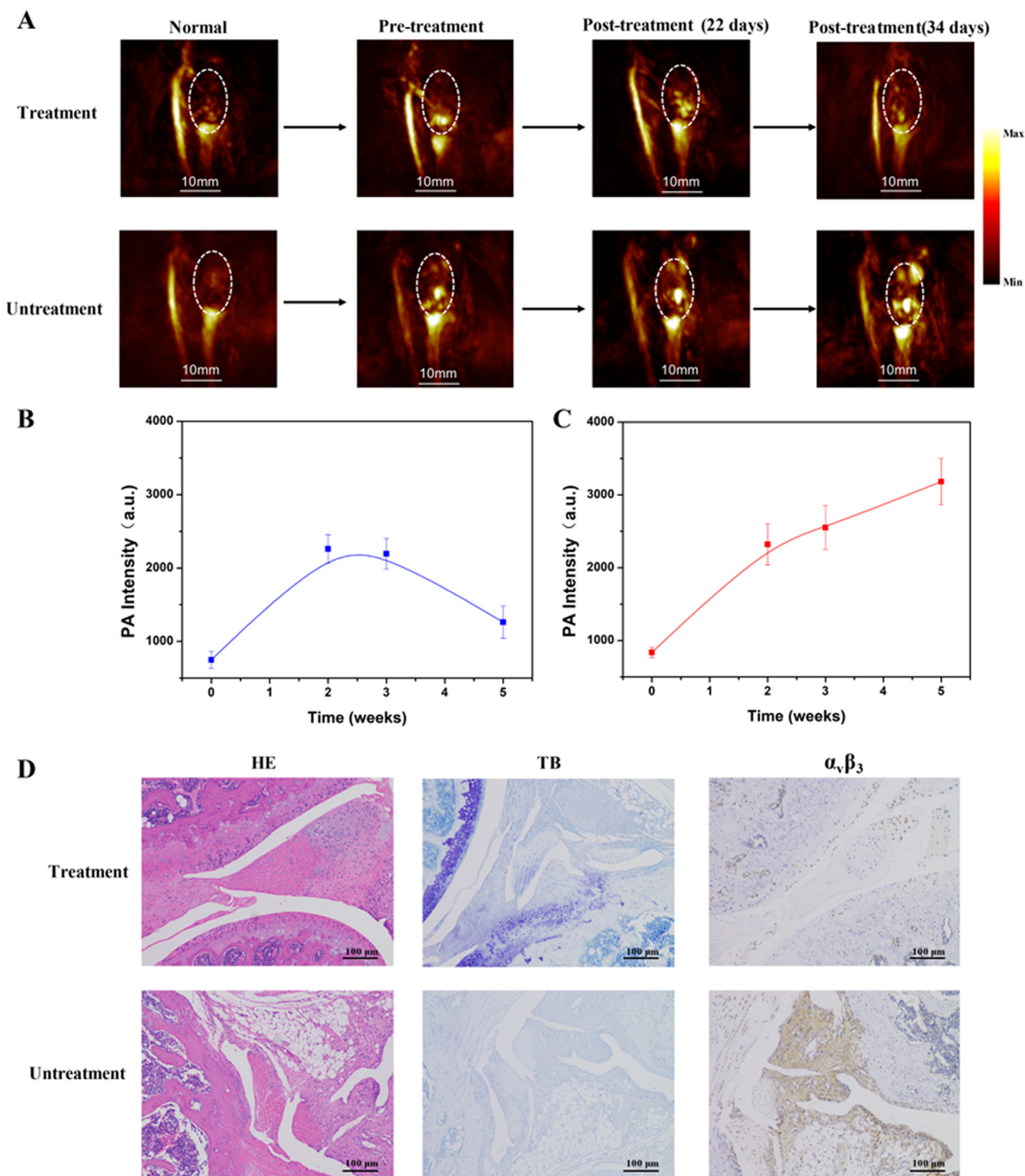


Fig. 8. The feasibility of MNP-PEG-RGD in monitoring RA therapeutic efficacy. (A) Representative PA images of treatment and un-treatment group (3 h after i.v. injection of MNP-PEG-RGD). Scale bar is 10 mm. (B) The PA intensity of treatment group (n = 5/group). (C) The PA intensity of un-treatment group (n = 5/group). (D) Representative mice histologic joints appearance of H&E and TB staining of treatment and un-treatment knee joints. IHC of $\alpha_v\beta_3$ -integrin. All the scale bar is 100 μ m.

radiological examination and the lack monitoring methods of RA, tracking RA progression in animals largely relied on histological examinations. It hinders early clinical intervention. It was particularly exciting to timely detect ERA and observe a steady increase in PA intensity during RA development, while significant differences could also be distinguished between stages.

Furthermore, we investigated the expression of $\alpha_v\beta_3$ -integrin in knee joint, which was also known as an indicator of progressive neovascularization. High $\alpha_v\beta_3$ activity was observed both in and *peri*-joint from RA mice, while only a slight expression of $\alpha_v\beta_3$ -integrin was detected in normal mice (Fig. 7A). Moreover, we found a notably increase in angiogenesis from early to developed stage of RA (Fig. 7D, $p < 0.01$). The observed enhanced PA signals *in vivo* were corresponding well with examined IHC of $\alpha_v\beta_3$ -integrin expression in RA joint.

3.6. Therapeutic monitoring

Considering the great behavior of MNP-PEG-RGD *in vivo* to detect different stages of RA, we further explored the MNP-PEG-RGD's ability to monitor the therapeutic efficacy of etanercept, a clinical drug to manage RA. RA mice were divided into two groups: untreated mice and treated mice. Before the treatment, PA signal intensity had similar raising trend in the two groups after RA induction (Fig. 8B & 8C). The treated group of mice was administered with etanercept starting from day 12 post AIA induction. Intriguingly, PA signals were much brighter in the untreated group than the treated group at 22 days (Fig. 8A). This finding also reflected the good therapeutic efficacy of etanercept in early intervention. In contrast to untreated RA mice, the intensity of PA signal was moderately declined after etanercept treatment (Fig. 8B). It was noteworthy that the therapeutic response could be quantified by calculating the intensities of PA signals in a timely manner. Moreover, we performed histological analysis and IHC of PA imaged RA mice, correlating PA signals with histological parameters and IHC known to demonstrate the disease progression. In the treatment group, the cartilage integrity was preserved with reduced levels of destruction and proteoglycan depletion (Fig. 8D). A clear interface between bone and cartilage was exhibited in Fig. 8D. Remarkably, in comparison to the synovial hypertrophy with neutrophils infiltration in untreated group (Fig. 8D), it was less detected in the treatment group with etanercept. These findings observed in histological analysis suggested that etanercept had an effective therapeutic effect in alleviating RA, which could also be assessed by MNP-PEG-RGD-enhanced PAI. IHC had shown that $\alpha_v\beta_3$ -integrin was predominantly found in the strongly degeneration of RA joint from untreated group, whereas the activity of $\alpha_v\beta_3$ -integrin was reduced in treatment group (Fig. 8D). The result shown in IHC correlated well with the PA intensity variations exhibited in PA images (Fig. 8A). Taken together, it was particularly exciting that MNP-PEG-RGD-enhanced PAI accurately and non-invasively monitored the therapeutic response in RA mice, which was attributed to the favorable PA property of MNP-PEG-RGD and active targeting towards $\alpha_v\beta_3$ -integrin.

3.7. Biodistribution and *in vivo* toxicity

We evaluated the metabolism biodistribution behavior of MNP-PEG-RGD in mice by *ex vivo* PAI. The extracted heart, liver, spleen, lung, kidney and bone after injection of MNP-PEG-RGD and PBS were embedded into agarose gel for PAI. Representative PA images were shown in Fig. S3A. The PA intensity measurements at day 1 indicated that more MNP-PEG-RGD accumulated in the liver and spleen after injection than that from PBS, implying the uptake of nanoparticles by phagocytic cells in the reticuloendothelial system (RES) (Fig. S3B). The decreased signal from liver and spleen may

suggest that MNP-PEG-RGD were gradually cleared from body 7 days after systemic administration to avoid accumulation *in vivo*.

Potential toxic effect and safety of nanoparticles are always a matter of great concern when scientists consider it translating into clinical use. MTT assay result mentioned above showed negligible cytotoxicity of MNP-PEG-RGD up to $100 \mu\text{g mL}^{-1}$. To further estimate the long-term toxicity of these nanomaterials, we conducted histological examinations of the major organs (heart, liver, spleen, lung and kidney) of normal mice at day 7 after *i.v.* injection on a daily basis. PBS- and MNP-PEG-RGD-treated normal mice showed no significant changes in tissue structures with no apparent cell necrosis or inflammatory infiltrate (Fig. S4B). Intra-articularly injection of MNP-PEG-RGD was also performed to detect its influence in joint. No resulting adverse clinical symptoms were observed and no obvious difference of joint between PBS and MNP-PEG-RGD injected groups demonstrating in H&E staining (Fig. S4A).

As depicted in Fig. S4C, no significant difference in the body weight was observed between PBS- and MNP-PEG-RGD-treated mice, demonstrating that MNP-PEG-RGD did not induce serious side effect. These results further validated the non-toxic nature of MNP-PEG-RGD. Favorable biodistribution and minimal impacts on animal viability without significant sign of toxicity further verify the practicality of MNP-PEG-RGD as a systemic probe for diagnostic molecular imaging *in vivo*.

4. Conclusion

In this study, we have demonstrated an application of MNP-PEG-RGD as an effective PA contrast agent for lightening ERA *in vivo*. MNP-PEG-RGD was facile synthesized with well biocompatible and had favorable PA properties. MNP-PEG-RGD can boost the PA signal at a low dose or living body visualization. MNP-PEG-RGD exhibited enhanced accumulation in the RA joints, which resulted in strong PA signals as early as 12 days since the RA induction. Moreover, MNP-PEG-RGD had an accurately staging capacity for clinics akin to clinical observations and histopathological analysis. Our study provides an effective method for monitoring the therapeutic efficacy on RA. The great biocompatibility of MNP-PEG-RGD holds attractive potential for clinical applications due to the excellent imaging performance. With further development, the novel platform of MNP-PEG-RGD can be used to simultaneously deliver treatment drug for RA precision therapy.

Declaration of Competing Interest

The authors declare that they have no known competing financial interests or personal relationships that could have appeared to influence the work reported in this paper.

Acknowledgements

This work was supported by the National Natural Science Foundation of China (No. 61905111); Wenzhou Municipal Science and Technology Bureau (CN) (No. Y20190266).

Data availability

The raw/processed data required to reproduce these findings cannot be shared at this time as the data also forms part of an ongoing study.

Appendix A. Supplementary material

Supplementary data to this article can be found online at <https://doi.org/10.1016/j.matdes.2021.109862>.

References

- [1] L.M. da Mota, C.V. Brenol, P. Palominos, R. Pinheiro Gda, Rheumatoid arthritis in Latin America: the importance of an early diagnosis, *Clin. Rheumatol.* 34 (Suppl 1) (2015) S29–S44.
- [2] I.E. van der Horst-Bruinsma, I. Speyer, H. Visser, F.C. Breedveld, J.M. Hazes, Diagnosis and course of early-onset arthritis: results of a special early arthritis clinic compared to routine patient care, *Br. J. Rheumatol.* 37 (10) (1998) 1084–1088.
- [3] I. Sudol-Szopinska, L. Jans, J. Teh, Rheumatoid arthritis: what do MRI and ultrasound show, *J. Ultrason.* 17 (68) (2017) 5–16.
- [4] F. Yan, Y. Sun, Y. Mao, M. Wu, Z. Deng, S. Li, X. Liu, L. Xue, H. Zheng, Ultrasound molecular imaging of atherosclerosis for early diagnosis and therapeutic evaluation through leucocyte-like multiple targeted microbubbles, *Theranostics* 8 (7) (2018) 1879–1891.
- [5] R. Weissleder, Molecular imaging in cancer, *Science* 312 (5777) (2006) 1168–1171.
- [6] J. Huang, J. Li, Y. Lyu, Q. Miao, K. Pu, Molecular optical imaging probes for early diagnosis of drug-induced acute kidney injury, *Nat. Mater.* 18 (10) (2019) 1133–1143.
- [7] J. Yao, L.V. Wang, Recent progress in photoacoustic molecular imaging, *Curr. Opin. Chem. Biol.* 45 (2018) 104–112.
- [8] L. Wang, P. Lei, X. Wen, P. Zhang, S. Yang, Tapered fiber-based intravascular photoacoustic endoscopy for high-resolution and deep-penetration imaging of lipid-rich plaque, *Opt. Express* 27 (9) (2019) 12832–12840.
- [9] L.V. Wang, S. Hu, Photoacoustic tomography: in vivo imaging from organelles to organs, *Science* 335 (6075) (2012) 1458–1462.
- [10] J.T. Friedlein, E. Baumann, K.A. Briggman, G.M. Colacion, F.R. Giorgetta, A.M. Goldfain, D.I. Herman, E.V. Hoenig, J. Hwang, N.R. Newbury, E.F. Perez, C.S. Yung, I. Coddington, K.C. Cossel, Dual-comb photoacoustic spectroscopy, *Nat. Commun.* 11 (1) (2020) 3152.
- [11] P. Burgholzer, J. Bauer-Marschallinger, M. Haltmeier, Breaking the resolution limit in photoacoustic imaging using non-negativity and sparsity, *Photoacoustics* 19 (2020) 100191.
- [12] T. Sowers, S. Emelianov, Exogenous imaging contrast and therapeutic agents for intravascular photoacoustic imaging and image-guided therapy, *Phys. Med. Biol.* 63 (22) (2018) 22TR01.
- [13] R.J. Paproski, A. Forbrich, E. Huynh, J. Chen, J.D. Lewis, G. Zheng, R.J. Zemp, Porphyrin nanodroplets: sub-micrometer ultrasound and photoacoustic contrast imaging agents, *Small* 12 (3) (2016) 371–380.
- [14] R. Nagaoka, T. Tabata, S. Yoshizawa, S.I. Umemura, Y. Saijo, Visualization of murine lymph vessels using photoacoustic imaging with contrast agents, *Photoacoustics* 9 (2018) 39–48.
- [15] J. Yu, H.N.Y. Nguyen, W. Steenberg, K. Kim, Recent development of technology and application of photoacoustic molecular imaging toward clinical translation, *J. Nucl. Med.* 59 (8) (2018) 1202–1207.
- [16] K. Sivasubramanian, V. Periyasamy, M. Pramanik, Non-invasive sentinel lymph node mapping and needle guidance using clinical handheld photoacoustic imaging system in small animal, *J. Biophotonics* 11 (1) (2018).
- [17] R. Sheikh, M. Cinthio, U. Dahlstrand, T. Erlov, M. Naumovska, B. Hammar, S. Zackrisson, T. Jansson, N. Reistad, M. Malmsjo, Clinical translation of a novel photoacoustic imaging system for examining the temporal artery, *IEEE Trans. Ultrason. Ferroelectr. Freq. Control* 66 (3) (2019) 472–480.
- [18] J. Jo, C.H. Lee, J. Folz, J.W.Y. Tan, X. Wang, R. Kopelman, In vivo photoacoustic lifetime based oxygen imaging with tumor targeted G2 polyacrylamide nanosonophores, *ACS Nano* 13 (12) (2019) 14024–14032.
- [19] B. Guo, J. Chen, N. Chen, E. Middha, S. Xu, Y. Pan, M. Wu, K. Li, C. Liu, B. Liu, High-resolution 3D NIR-II photoacoustic imaging of cerebral and tumor vasculatures using conjugated polymer nanoparticles as contrast agent, *Adv. Mater.* 31 (25) (2019) e1808355.
- [20] H. Ding, Y. Cai, L. Gao, M. Liang, B. Miao, H. Wu, Y. Liu, N. Xie, A. Tang, K. Fan, X. Yan, G. Nie, Exosome-like nanozyme vesicles for H₂O₂-responsive catalytic photoacoustic imaging of xenograft nasopharyngeal carcinoma, *Nano Lett.* 19 (1) (2019) 203–209.
- [21] H. Gong, R. Peng, Z. Liu, Carbon nanotubes for biomedical imaging: the recent advances, *Adv. Drug Deliv. Rev.* 65 (15) (2013) 1951–1963.
- [22] A. De la Zerde, C. Zavaleta, S. Keren, S. Vaithilingam, S. Bodapati, Z. Liu, J. Levi, B.R. Smith, T.J. Ma, O. Oralkan, Z. Cheng, X. Chen, H. Dai, B.T. Khuri-Yakub, S.S. Gambhir, Carbon nanotubes as photoacoustic molecular imaging agents in living mice, *Nat. Nanotechnol.* 3 (9) (2008) 557–562.
- [23] L. Cui, J. Rao, Semiconducting polymer nanoparticles as photoacoustic molecular imaging probes, *Wiley Interdiscip. Rev. Nanomed. Nanobiotechnol.* 9 (2) (2017).
- [24] Q. Fu, R. Zhu, J. Song, H. Yang, X. Chen, Photoacoustic imaging: contrast agents and their biomedical applications, *Adv. Mater.* 31 (6) (2019) e1805875.
- [25] R. Hou, X. Liu, K. Xiang, L. Chen, X. Wu, W. Lin, M. Zheng, J. Fu, Characterization of the physicochemical properties and extraction optimization of natural melanin from *Inonotus hispidus* mushroom, *Food Chem.* 277 (2019) 533–542.
- [26] D.J. Harper, T. Konegger, M. Augustin, K. Schutzenberger, P. Eugui, A. Lichtenegger, C.W. Merkle, C.K. Hitzberger, M. Glosmann, B. Baumann, Hyperspectral optical coherence tomography for in vivo visualization of melanin in the retinal pigment epithelium, *J. Biophotonics* 12 (12) (2019) e201900153.
- [27] W. Wang, T. Jing, X. Xia, L. Tang, Z. Huang, F. Liu, Z. Wang, H. Ran, M. Li, J. Xia, Melanin-loaded biocompatible photosensitive nanoparticles for controlled drug release in combined photothermal-chemotherapy guided by photoacoustic/ultrasound dual-modality imaging, *Biomater. Sci.* 7 (10) (2019) 4060–4074.
- [28] T. Sun, D. Jiang, Z.T. Rosenkrans, E.B. Ehlerding, D. Ni, C. Qi, C.J. Kuttyreff, T.E. Barnhart, J.W. Engle, P. Huang, W. Cai, A melanin-based natural antioxidant defense nanosystem for theranostic application in acute kidney injury, *Adv. Funct. Mater.* 29 (48) (2019).
- [29] L. Zhang, D. Sheng, D. Wang, Y. Yao, K. Yang, Z. Wang, L. Deng, Y. Chen, Bioinspired multifunctional melanin-based nanoliposome for photoacoustic/magnetic resonance imaging-guided efficient photothermal ablation of cancer, *Theranostics* 8 (6) (2018) 1591–1606.
- [30] J. Huang, F. Liu, X. Han, L. Zhang, Z. Hu, Q. Jiang, Z. Wang, H. Ran, D. Wang, P. Li, Nanosensitizers for highly efficient sonodynamic cancer theranostics, *Theranostics* 8 (22) (2018) 6178–6194.
- [31] Q. Fan, K. Cheng, X. Hu, X. Ma, R. Zhang, M. Yang, X. Lu, L. Xing, W. Huang, S.S. Gambhir, Z. Cheng, Transferring biomarker into molecular probe: melanin nanoparticle as a naturally active platform for multimodality imaging, *J. Am. Chem. Soc.* 136 (43) (2014) 15185–15194.
- [32] H.A. Elshabrawy, Z. Chen, M.V. Volin, S. Ravella, S. Virupannavar, S. Shahrara, The pathogenic role of angiogenesis in rheumatoid arthritis, *Angiogenesis* 18 (4) (2015) 433–448.
- [33] D.G. Stupack, C.M. Storgard, D.A. Cheresh, A role for angiogenesis in rheumatoid arthritis, *Braz. J. Med. Biol. Res.* 32 (5) (1999) 573–581.
- [34] B.A. Johnson, G.K. Haines, L.A. Harlow, A.E. Koch, Adhesion molecule expression in human synovial tissue, *Arthritis Rheum.* 36 (2) (1993) 137–146.
- [35] R. Siitonen, E. Peuhu, A. Autio, H. Liljenback, E. Mattila, O. Metsala, M. Kakela, T. Saanijoki, I. Dijkgraaf, S. Jalkanen, J. Ivaska, A. Roivainen, (68)Ga-DOTA-EJC (RGDFK)2 PET imaging of SHARPIN-regulated integrin activity in mice, *J. Nucl. Med.* 60 (10) (2019) 1380–1387.
- [36] C. Mas-Moruno, R. Fraioli, F. Rechenmacher, S. Neubauer, T.G. Kapp, H. Kessler, alpha5beta3- or alpha5beta1-integrin-selective peptidomimetics for surface coating, *Angew. Chem. Int. Ed. Engl.* 55 (25) (2016) 7048–7067.
- [37] A. Dayan, G. Fleminger, O. Ashur-Fabian, Targeting the Achilles' heel of cancer cells via integrin-mediated delivery of ROS-generating dihydroloamide dehydrogenase, *Oncogene* 38 (25) (2019) 5050–5061.
- [38] M.A. Lewandowski, M.W. Hinz, A simple approach to industrial laser safety, *Health Phys.* 88 (2 Suppl) (2005) S24–S30.
- [39] M. Barbalinardo, F. Caicci, M. Cavallini, D. Gentili, Protein corona mediated uptake and cytotoxicity of silver nanoparticles in mouse embryonic fibroblast, *Small* 14 (34) (2018) e1801219.
- [40] L. Qiu, Q. Hu, L. Cheng, L. Li, C. Tian, W. Chen, Q. Chen, W. Hu, L. Xu, J. Yang, L. Cheng, D. Chen, cRGDYK modified pH responsive nanoparticles for specific intracellular delivery of doxorubicin, *Acta Biomater.* 30 (2016) 285–298.
- [41] R. Chakravarty, S. Chakraborty, A. Guleria, C. Kumar, A. Kunwar, K.V.V. Nair, H. D. Sarma, A. Dash, Clinical scale synthesis of intrinsically radiolabeled and cyclic RGD peptide functionalized (198)Au nanoparticles for targeted cancer therapy, *Nucl. Med. Biol.* 72–73 (2019) 1–10.
- [42] T. Kamala, Hock immunization: a humane alternative to mouse footprint injections, *J. Immunol. Methods* 328 (1–2) (2007) 204–214.
- [43] J. Zhao, M. Zhao, C. Yu, X. Zhang, J. Liu, X. Cheng, R.J. Lee, F. Sun, L. Teng, Y. Li, Multifunctional folate receptor-targeting and pH-responsive nanocarriers loaded with methotrexate for treatment of rheumatoid arthritis, *Int J Nanomedicine* 12 (2017) 6735–6746.
- [44] D.D. Brand, K.A. Latham, E.F. Rosloniec, Collagen-induced arthritis, *Nat. Protoc.* 2 (5) (2007) 1269–1275.
- [45] N. Beziere, C. von Schacky, Y. Kosanke, M. Kimm, A. Nunes, K. Licha, M. Aichler, A. Walch, E.J. Rummeny, V. Ntziachristos, R. Meier, Optoacoustic imaging and staging of inflammation in a murine model of arthritis, *Arthritis Rheumatol.* 66 (8) (2014) 2071–2078.
- [46] C. Liu, L. He, J. Wang, Q. Wang, C. Sun, Y. Li, K. Jia, J. Wang, T. Xu, R. Ming, Q. Wang, N. Lin, Anti-angiogenic effect of Shikonin in rheumatoid arthritis by downregulating PI3K/AKT and MAPKs signaling pathways, *J. Ethnopharmacol.* 260 (2020) 113039.
- [47] A.M. Roccaro, F. Russo, T. Cirulli, G. Di Pietro, A. Vacca, F. Dammacco, Antiangiogenesis for rheumatoid arthritis, *Curr. Drug Targets Inflamm. Allergy* 4 (1) (2005) 27–30.
- [48] H.F. Zhou, G. Hu, S.A. Wickline, G.M. Lanza, C.T. Pham, Synergistic effect of antiangiogenic nanotherapy combined with methotrexate in the treatment of experimental inflammatory arthritis, *Nanomedicine (Lond)* 5 (7) (2010) 1065–1074.
- [49] Y. Lu, L. Li, Z. Lin, L. Wang, L. Lin, M. Li, Y. Zhang, Q. Yin, Q. Li, H. Xia, A new treatment modality for rheumatoid arthritis: combined photothermal and photodynamic therapy using Cu₇S₄ nanoparticles, *Adv. Healthc. Mater.* 7 (14) (2018) e1800013.
- [50] L. Liu, F. Hu, H. Wang, X. Wu, A.S. Eltahan, S. Stanford, N. Bottini, H. Xiao, M. Bottini, W. Guo, X.J. Liang, Secreted protein acidic and rich in cysteine mediated biomimetic delivery of methotrexate by albumin-based nanomedicines for rheumatoid arthritis therapy, *ACS Nano* 13 (5) (2019) 5036–5048.